minerals

MDPI

Article

Numerical Simulation and Optimization of Screening Process for Vibrating Flip-Flow Screen Based on Discrete Element Method–Finite Element Method–Multi-Body Dynamics Coupling Method

Ningning Xu [1,*], Xinwen Wang [1], Dongdong Lin [1] and Weiran Zuo [2]

[1] School of Chemical & Environmental Engineering, China University of Mining and Technology-Beijing, Beijing 100083, China; xinwen.w@cumtb.edu.cn (X.W.); ldd@student.cumtb.edu.cn (D.L.)
[2] Zijin School of Geology and Mining, Fuzhou University, Fuzhou 350108, China; zuoweiran@fzu.edu.cn
* Correspondence: bqt1900301010@student.cumtb.edu.cn

Abstract: Vibrating flip-flow screens are widely employed in the deep screening processes of coal washing, solid waste treatment, metallurgy, and other fields, playing a crucial role in enhancing product quality and production efficiency. The screen surface and material movement of vibrating flip-flow screens are highly complex, and there is currently insufficient understanding of their screening mechanism, limiting further optimization and application. In this paper, the Discrete Element Method (DEM), Finite Element Method (FEM), and Multi-Body Dynamics (MBD) were integrated to establish a numerical coupling model for vibrating flip-flow screens, considering material loads, screen surface deformation, and screen machine dynamics. The Response Surface Method was utilized to analyze the significant impact of relative amplitude, tension amount, amplitude of driving screen frame, vibration frequency, and screen surface inclination on screening efficiency and material velocity. The results indicate that the most significant factor influencing the screening of flip-flow screens is the screen surface inclination. Based on a BP neural network, a five-degree-of-freedom inclination surrogate model for flip-flow screens was established. The whale algorithm was employed for multi-objective optimization of the surrogate model, resulting in a screen surface inclination distribution that meets the requirements of different operating conditions.

Keywords: vibrating flip-flow screen; screening process; numerical coupling simulation; surrogate model; optimization design

check for updates

Citation: Xu, N.; Wang, X.; Lin, D.; Zuo, W. Numerical Simulation and Optimization of Screening Process for Vibrating Flip-Flow Screen Based on Discrete Element Method–Finite Element Method–Multi-Body Dynamics Coupling Method. *Minerals* **2024**, *14*, 278. https://doi.org/10.3390/min14030278

Academic Editor: Sunil Kumar Tripathy

Received: 22 January 2024
Revised: 26 February 2024
Accepted: 4 March 2024
Published: 6 March 2024

Copyright: © 2024 by the authors. Licensee MDPI, Basel, Switzerland. This article is an open access article distributed under the terms and conditions of the Creative Commons Attribution (CC BY) license (https://creativecommons.org/licenses/by/4.0/).

1. Introduction

Different from conventional vibrating screens, the vibrating flip-flow screen is a dual-body system with a driving screen frame and a driven screen frame. The exciter stimulates the driving screen frame, causing relative motion between the two screen frames. This, in turn, drives the flexible screen panel to undergo alternating large flexural deformations of tension and relaxation, completing the screening process for materials on the screen. The application of the flip-flow screen has been widespread. In coal preparation plants, its use has lowered the lower limit of screening classification from 13 mm to 3 mm, achieving the removal of fine-grained particles in the raw coal [1–3]. In metal ore production, the lower classification limit of the flip-flow screen provides material with higher grindability for high-pressure roller mills, realizing "more crushing, less grinding", thereby reducing the overall energy consumption of crushing and grinding [4]. In the process of construction waste treatment, the flip-flow screen is used to separate aggregates from sand, ensuring the quality and performance of aggregates as building materials [5]. However, various challenges have been encountered in the application of the flip-flow screen. Issues such as instability in the screening process when the material is overloaded, lower efficiency

in screening sticky and wet materials, and the design challenges of scaling up have been noted [6,7]. Moreover, the flexible screen plate and particle movement of the flip-flow screen are highly complex. Currently, there is insufficient understanding of its screening mechanism, which restricts its further optimization and application.

To optimize the screening process of the flip-flow screen, researchers have conducted relevant experimental studies. Li et al. [8] investigated the separation performance of the flip-flow screen at different drive frequencies and feed rates through screening experiments. The results indicate that as the drive frequency increases, the screening efficiency initially increases and then decreases, while an increase in feed rate gradually reduces the screening efficiency. Geng et al. [9] conducted intermediate-scale screening experiments, comparing the screening performance of the vibrating flip-flow screen with the circular vibrating screen for materials with different moisture content. The results show that when the material has a higher moisture content, the screening performance of the flip-flow screen is superior to that of the circular vibrating screen. To further analyze the screening process of the flip-flow screen, Wang et al. [10] used experimental methods to track the variation in the amount of quartz sand passing through a single flip-flow screen surface over time. Based on the throughput, the screening process was divided into two stages: rapid throughput and slow throughput. A model describing the variation in throughput velocity over time was fitted based on the experimental results. The aforementioned experimental studies qualitatively analyzed the influencing factors of the flip-flow screen, providing a macroscopic analysis of the screening process. However, these studies offer limited assistance in understanding the particle movement and screening mechanism on the flip-flow screen at a microscopic scale.

Numerical simulations based on the Discrete Element Method (DEM) [11–13] have provided an effective means for in-depth research into the screening process of the flip-flow screen. Yu et al. [14] approximated the deformation movement of the flexible screen plate by simulating the discrete motion of rigid bodies at multiple points. They investigated the influence of particle surface energy on screening efficiency, revealing that higher particle viscosity requires a longer screening distance. Wu et al. [15] also proposed a DEM-MBD (Discrete Element Method–Multi-Body Dynamics) bidirectional coupling method using a discretization approach to simulate the flexible screening process of the flip-flow screen. In comparison to the model proposed by Yu et al., this coupling model not only considers the excitation effect of the screen plate on particles but also takes into account the influence of particles on the amplitude of the screen plate. The research results indicate that screening efficiency and yield exhibit a nonlinear increase with the increase in excitation frequency. The impact of the screen surface elastic modulus on screening performance indicators is not significant. Zhang et al. [16], using this method, studied the effects of screen surface inclination and material composition on screening efficiency and material velocity. In their research, they found that material load causes a decrease in screen surface amplitude and vibration intensity. Tang et al. [17], based on DEM, established a realistic model of wet coal agglomerate particles and studied the collision and disaggregation process between wet coal agglomerates and the flexible screen plate. They analyzed the disaggregation mechanism and influencing factors. The aforementioned studies used an approximate stiffness simulation without considering the flexible deformation of the screen plate. To address this, Chen et al. [18] established a vibrating screen plate model using ABAQUS. This model not only considers the interaction between the screen plate and the material but also takes into account the flexible deformation of the screen surface, obtaining displacement data for various points on the screen plate during flexible motion. Xu et al. [19] developed a flip-flow screen DEM-FEM coupling model that considers the flexible deformation of the screen surface. However, this model still neglects the impact of material load on the dynamics of the screening machine, leading to significant errors when simulating material overload conditions. Nevertheless, in actual production, to achieve higher output, thick material layers conditions are often encountered. Therefore, it is necessary to further improve numerical models to simulate the screening of thick material layers on flip-flow screens.

There are many other studies related to DEM coupling simulations; for example, Dratt and Katterfeld [20] proposed a bidirectional coupling method using the finite element software ANSYS® Classic and the DEM software LIGHTTS® to achieve complex interactions between large bulk materials and highly deformable materials. Richter et al. [21] provided an explanation of the coupling interface between the DEM code LIGHTTS® and the multibody software. The simulation results were validated through simplified experiments with a bucket elevator. Clearly, these studies also provide feasible solutions for simulating the process of particle screening using flip-flow screens. However, to simulate the flip-flow screen with a thick material layer, it is necessary to analyze not only the flexible deformation of the flexible screen panel under heavy loads but also the dynamic impact of screen frame vibration caused by the tension and deformation of the screen panel. This involves the discrete element simulation of discrete material movement [22,23], finite element simulation of flexible screen panel deformation [24,25], and multibody dynamics simulation of screen frame vibration [26,27]. Therefore, a numerical model for the DEM-FEM-MBD coupling simulation of vibrating tensioned screens has been established in this study. It successfully simulated the screening process of the vibrating flip-flow screen from a thick material layer at the feeding end to a thin material layer at the discharge end. The accuracy of the numerical coupling model in simulating screening machine dynamics, screen surface slack deformation, and the screening process was validated through screening machine motion tests, screen surface vibration tests, and screening experiments. The significance of the relative amplitude, tensioning amount, amplitude of driving screen frame, vibration frequency, and screen surface inclination was analyzed. A five-degree-of-freedom inclination surrogate model for the flip-flow screen was established, and multi-objective optimization using the whale algorithm was employed to obtain the optimal inclination distribution of the screen surface under different operating conditions.

2. Materials and Methods

The dynamic model of the vibrating flip-flow screen, as shown in Figure 1, involves the vibration of the driving screen frame (M_1) and the driven screen frame (M_2), inducing slack deformation of the flexible screen plate. This, in turn, causes the material (M_3) on the screen plate to be thrown up, completing the screening. In this process, there is not only relative interaction between the material and the flexible screen surface [16] but also relative interaction between the flexible screen plate and the screen frame [28]. Therefore, a Multi-Body Dynamics (MBD) system for the vibrating flip-flow screen was established based on the DEM-FEM coupling numerical model. The aim was to consider the impact of changes in amplitude under material overload conditions on the screening process, thereby improving the accuracy of simulating the screening process of the vibrating flip-flow screen.

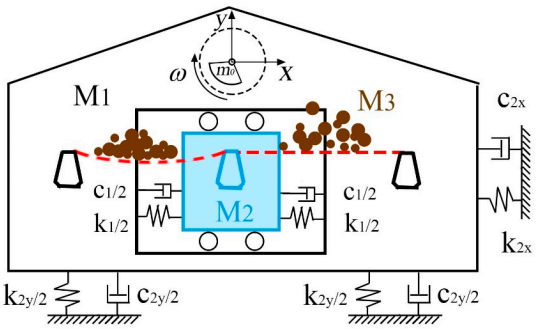


Figure 1. Dynamic model of the vibrating flip-flow screen.

In this study, the coupling between discrete particle (DEM) and screen surface (FEM) was achieved using the ABAQUS software (ABAQUS2019). The coupling method involved treating the discrete particles as particles and modeling their contact with the screen panel using the Hertz model, while the transfer of forces was calculated using shape functions. Please refer to reference [19] for a more detailed explanation. In this study, the authors

utilized the ABAQUS software to establish a dynamic model of the vibrating screen. By imposing boundary conditions, the forces on the screen panel were transmitted to the dynamic model of the screening machine. This allowed for the consideration of the impact of the material load on the motion of the screening machine. As a result, the discrete elements interacted with the screen panel through the Hertz model and shape functions, and the deformation of the screen panel influenced the dynamics of the screening machine, thereby achieving the interaction of forces among the three components. The DEM-FEM coupling method has been detailed in reference [19], and here we focus on the methods used for simulating the dynamics of the vibrating flip-flow screen.

2.1. Solution of Screening Machine Dynamics

The central difference method was employed to solve the overall equilibrium equation of the screening machine. The dynamic equation was applied to calculate the dynamic conditions of the next incremental step within each small increment. The overall screening machine model is composed of grids and nodes, with the mass matrix of each node denoted as M, acceleration as $\ddot{u}$, external force as P, and internal force of the element as I. Therefore, the equilibrium equation for each node is:

$$M\ddot{u} = P - I \tag{1}$$

The acceleration of the node at time t can be calculated from the above equation as:

$$\ddot{u} \mid (t) = (M)^{-1}(P - I)(t) \tag{2}$$

The screening machine motion process was decomposed into very short incremental steps. To accurately capture the high-speed movement characteristics of the vibrating flip-flow screen and the flexible screen plate, the smallest time increment was chosen to be $\Delta t = 8 \times 10^{-7}$ s. Ensuring computational stability and efficiency, assuming constant acceleration within this extremely short time, the velocity equation for nodes was calculated by integrating acceleration using the central difference method:

$$\dot{u}\left|\left(t + \frac{\Delta t}{2}\right) = \dot{u}\right|\left(t - \frac{\Delta t}{2}\right) + \frac{(\Delta t|(t + \Delta t) + \Delta t|(t))}{2}\ddot{u}(t) \tag{3}$$

Applying the central difference method again, the displacement equation was solved by integrating velocity:

$$u\left|(t + \Delta t) = u\right|(t) + \Delta t\left|(t + \Delta t)\dot{u}\right|\left(t + \frac{\Delta t}{2}\right) \tag{4}$$

2.2. Particle Motion and Contact

In the coupling model, each discrete particle is represented by a PD3D element with translational and rotational degrees of freedom. Its motion is described by Newton's second law, calculated separately by Equations (5) and (6) for the translational and rotational motion of each particle.

$$\dot{v}_p = \frac{\sum F_p}{m_p} + g \tag{5}$$

$$\dot{\omega}_p = \frac{\sum M_p}{I_p} \tag{6}$$

where m_p and g are the mass and gravitational acceleration of the particle, respectively; ω_p is the angular velocity vector; M_p and I_p are the tangential force and torque caused by rotational inertia, respectively; v_p is the particle velocity vector; and F_p is the contact force acting on the particle. By integrating the above expressions and distinguishing between

different forces acting on the particle (contact force and gravitational force), the velocity and trajectory of each particle can be determined.

When calculating the contact force between particles, considering the capillary forces between wet and sticky material particles, the Hertz–Mindlin–JKR model [29], an extension of the Hertz–Mindlin model [30,31], was adopted as the contact force model between particles. The calculation method follows reference [19], and the setting of contact parameters between particles is in accordance with reference [32].

2.3. Model Structure and Grid Partition

The FFS0827 experimental screen, as shown in Figure 2, has a highly complex structure. To enhance computational efficiency in simulation, while ensuring the mass, rotational inertia, and center of mass of the vibrating body remain unchanged, the original model has been simplified. The simplification mainly focused on the driving screen frame, driven screen frame, and exciter involved in the vibration. Details such as screw holes, lifting lugs, and chamfers that do not affect the vibration and screening of the screening machine were removed, facilitating grid partitioning and simultaneously saving computational resources. Figure 2 illustrates the process and results of the model simplification for the experimental screen. Figure 2c shows the dimensions of the whole screen surface, a single screen panel, and the screen apertures.

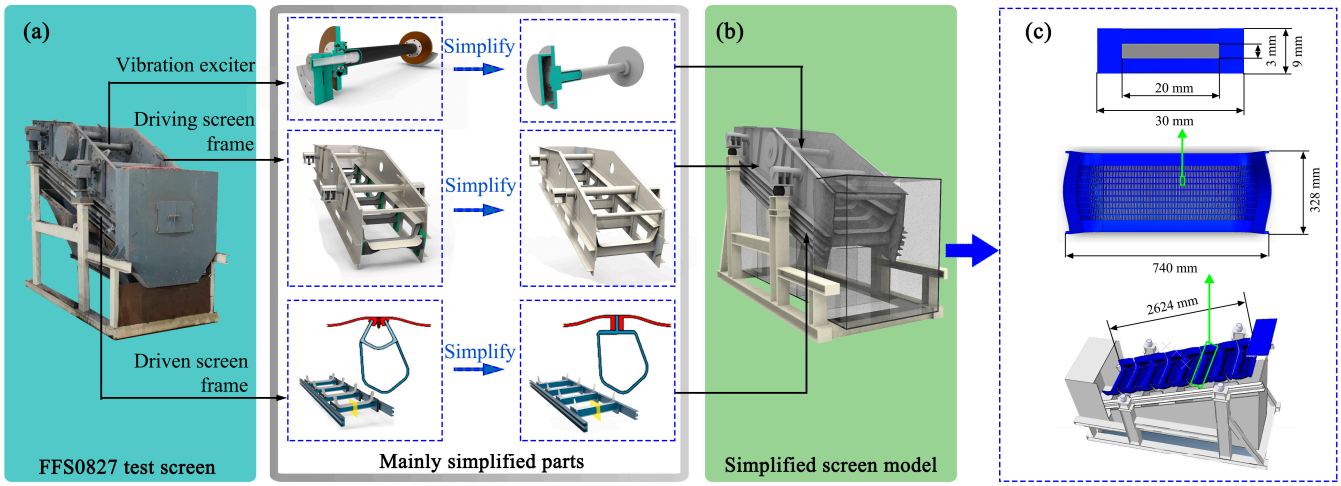


Figure 2. Simplification of the structural model of the FFS0827 experimental screen: (**a**) testing machine; (**b**) simplified model; (**c**) main dimensions.

Finite element analysis discretizes complex structures into a series of small elements or units through grid partitioning, enabling approximate solutions to complex problems. Figure 3 shows the grid partitioning for the exciter, driven screen frame, driving screen frame, and flexible screen plate. For the exciter with many curved surfaces and the structurally complex driving screen frame, tetrahedral grids with strong adaptability were used for partitioning. For the relatively regular structure of the driven screen frame and the flexible screen surface, hexahedral grids with higher computational efficiency were employed. The screen plate is a major deformable component, experiencing significant deflection during motion and featuring small structural details such as 3 mm screen holes. Its motion and deformation directly impact particle movement and the screening process. Therefore, optimizing the grid for the screen plate is beneficial for improving computational speed and accuracy. As shown in Figure 3d, a local refinement method was applied to partition the screen plate. Coarse grids were used in areas without screen holes on both sides of the slack screen surface, and refinement grids were applied at bending points and screen holes, while transition grids of moderate size were used between them. However, unavoidably, the screen plate has a porous shape, and ensuring grid quality inevitably results in a larger number of elements. In this grid partitioning, each screen plate has 5062 elements.

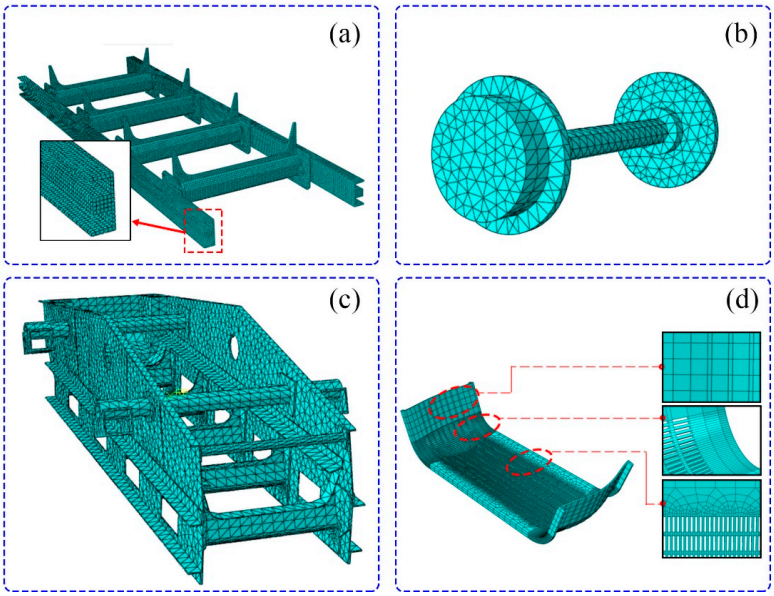


Figure 3. Grid partitioning results for various parts of the screening machine: (**a**) driven screen frame; (**b**) exciter; (**c**) driving screen frame; (**d**) screen plate.

2.4. Numerical Model of Rubber Springs

In ABAQUS, the provided Bushing element allows the setting of stiffness and damping in various directions, enabling the simulation of shear springs with rubber material. The schematic diagram of the rubber spring model is shown in Figure 4a. The stiffness and damping parameters of the rubber spring provided by the manufacturer are listed in Table 1. Based on these parameters, the stiffness and damping parameters of the Bushing connector were configured. Figure 4b illustrates the numerical model of the shear spring established using the Bushing element, with Steel Plate 2 fixed and a sinusoidal displacement applied to Steel Plate 1 in the X-direction. A comparison with experimental results under the same conditions is presented in Figure 5a. The experimental data were obtained using the tensile tester (INSTRON 8801) as shown in Figure 5b. The hysteresis curve of the numerical shear spring model fits well with the experimental results, effectively reflecting the stiffness and damping characteristics of the shear spring.

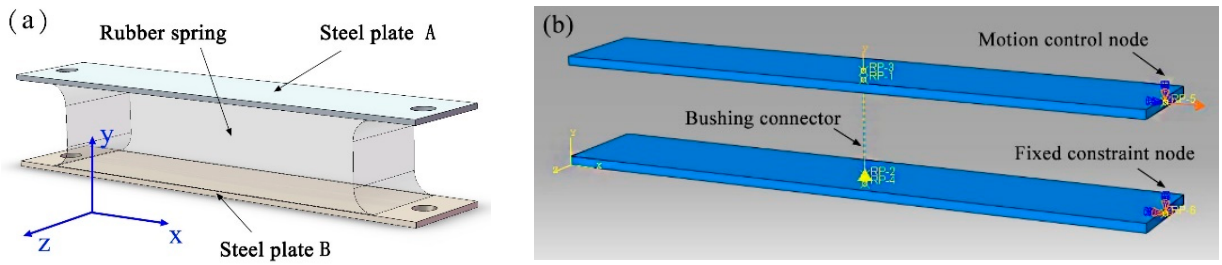


Figure 4. Rubber spring: (**a**) structure diagram; (**b**) numerical model.

Table 1. Rubber spring parameters.

Direction	Stiffness (N/m)	Damping (N·s/m)
x	225,000	12.5
y	5,000,000	37.5
z	225,000	12.5

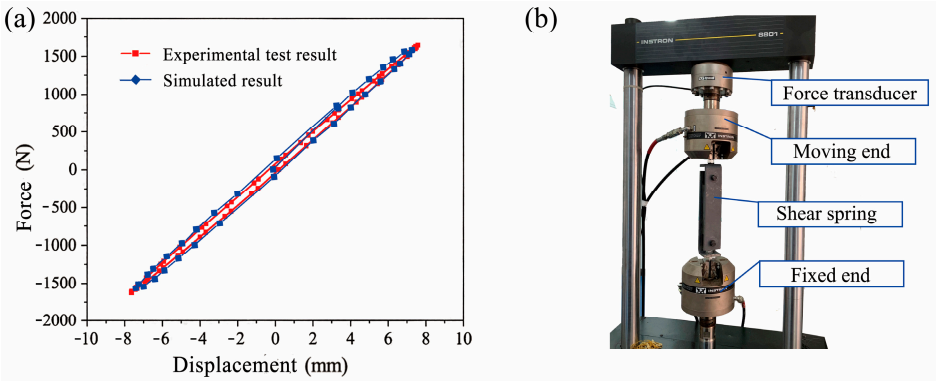


Figure 5. Comparison between test results and simulation results of the shear spring hysteresis curve: (**a**) comparison result; (**b**) test device.

2.5. The Simulation of the Flexible Screen Panel

The flip-flow screen surface is made of polyurethane elastomer material, which is a hyperelastic material exhibiting mechanical properties such as elastic deformation, incompressibility, and nonlinearity. During the operation of the vibrating screen surface, it undergoes elastic deformation under the stretching effect of the screen frame and is influenced by the apertures of the screen panel, with the deformation primarily dominated by uniaxial tension at the locations of the screen panel apertures. When the tensile strain does not exceed 100% and the compressive strain does not exceed 30%, the two-parameter Mooney–Rivlin model can effectively describe the hyperelastic material's mechanical behavior [33]. The stretching of the vibrating screen surface is approximately 2.5%. Therefore, in this study, the Mooney–Rivlin model with two parameters was selected for finite element analysis of the vibrating screen surface. The two-parameter Mooney–Rivlin model is represented by Equation (7).

$$W = C_{10}(I_1 - 3) + C_{01}(I_2 - 3) + \frac{1}{D_1}(J - 1)^2 \tag{7}$$

where C_{ij} represents the material constants, D_1 is the incompressibility parameter, J is the volume change rate, and I_1 and I_2 are the first and second deformation tensor invariants, respectively. The material parameters are shown in Table 2.

Table 2. Mooney–Rivlin model parameters.

Parameter	Value
C_{01}	2.8×10^6
C_{10}	7×10^5
D_1	0.001

2.6. Setting Boundary Conditions

In order to obtain a realistic simulation of the dynamic behavior and screening process of the FFS0827 experimental screen, numerical virtual prototype boundary conditions were set based on the actual situation of the FFS0827 experimental screen, as shown in Figure 6. This mainly includes the following motion constraints and external loads:

(1) Fixed constraints: The support frame and feed chute were fixed to the bottom surface, and the material inlet chute was fixed above the feeding end of the screening machine. These components do not participate in the vibration of the screening machine.
(2) Rigid body constraints: To improve computational efficiency, rigid body constraints were applied to components such as the driving screen frame, driven screen frame, support frame, and material blocking plate, excluding the screen plate undergoing flexible deformation. Their flexible deformation is not considered.

(3) Binding constraints: The exciter and sealing plate vibrate together with the driving screen frame. Therefore, binding constraints were applied between the exciter and the main screen frame. The flexible screen plates were bound at both ends to connect with the driving screen frame and the driven screen frame.
(4) Gravity load: A gravity field was set throughout the entire computational domain.
(5) Excitation force load: The excitation force load was applied at both ends of the central axis of the exciter, simulating the centrifugal inertia force of the eccentric block through orthogonal and opposite-phase sinusoidal forces. The mass moment of the eccentric block in the experimental screen is 3.5 kg·m, and with a rotation speed of ω, the excitation force $F = 3.5\omega^2$.
(6) Elastic elements: Four Bushing elements connect the driving screen frame to the frame, and three sets of Bushing elements connect the driven screen frame to the driving screen frame.

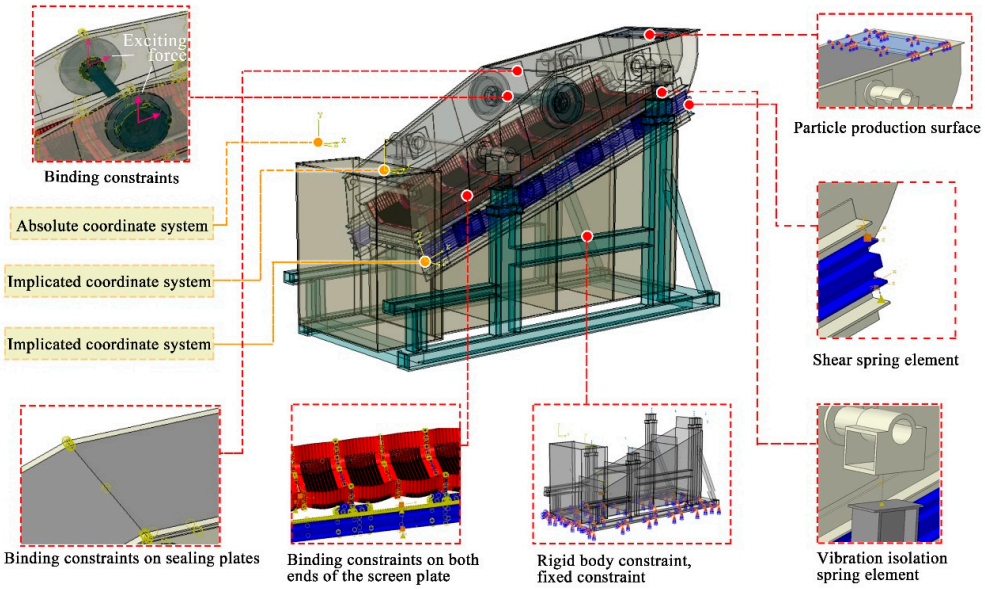


Figure 6. Boundary conditions and external load settings.

After completing the establishment of the structural model, mesh division, setting of boundary conditions, and configuration of external loads, a particle material feeding velocity of 40 kg/s was set in the DEM-FEM coupling program. The particle size distribution is illustrated in Figure 7. The particle parameters were set according to Table 3, and the calibration process followed reference [32]. Due to the use of the same material, the specific calibration process will not be reiterated here. The simulated screening process is depicted in Figure 8 and results in an average thickness of the material layer of approximately 175 mm.

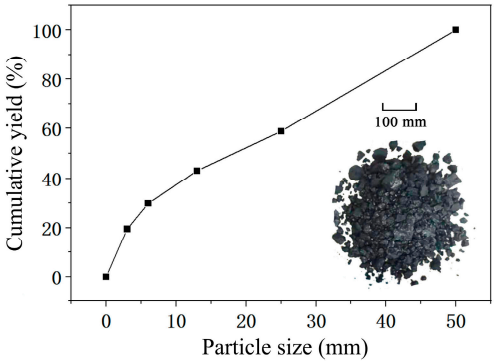


Figure 7. Particle size composition.

Table 3. DEM parameters.

Object	Parameter	Value
Particle	Density	1430
	Modulus of elasticity	9.9×10^8
	Poisson's ratio	0.3
Between particles and the screen surface	JKR	7.75
	Recovery coefficient	0.34
	Coefficient of rolling friction	0.09
	Coefficient of sliding friction	0.47
Between particles	JKR	12.86
	Recovery coefficient	0.13
	Coefficient of rolling friction	0.08
	Coefficient of sliding friction	0.36

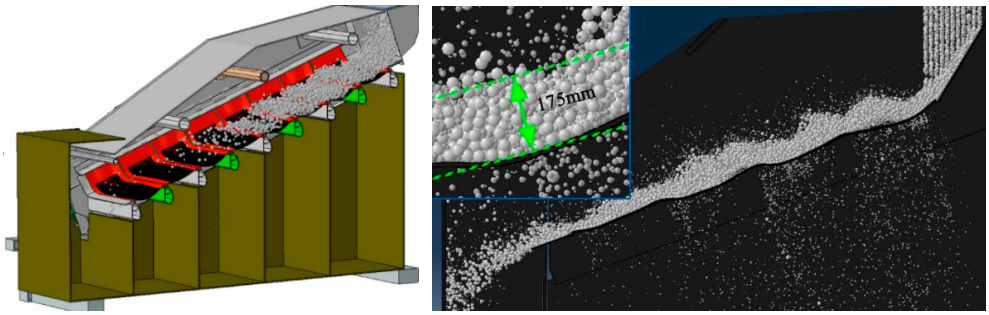


Figure 8. Simulation of vibrating flip-flow screen screening.

3. Experimental Validation of Numerical Coupling Models

In order to analyze whether the flip-flow screen DEM-FEM-MBD coupling model established in this paper can effectively reflect the basic characteristics of the experimental screen, experiments on the amplitude of the screen plate, the motion of the screen frame, and the screening process were conducted. The accuracy of the simulation was verified in terms of three aspects: the deformation of the finite element screen plates, the dynamics of the screen frames, and the particles screening process.

3.1. Experimental Validation of Screen Plate Deformation

Figure 9 depicts the schematic diagram of the displacement test experiment for the screen plate of the flip-flow screen. Acceleration sensors were securely fastened to the flexible screen plate with screws, and tests were conducted on a total of 12 points on the screen surface along the direction of relative motion. The aim was to describe the motion and deformation process of the screen surface. Ultimately, the amplitudes of each point on the screen surface were obtained through signal acquisition equipment and upper computer processing. The experimental test results were compared with the simulation results, as illustrated in Figure 10. The figures present the shapes of the flexible screen plate at four moments within one vibration cycle. The green color represents the numerical simulation results, and the red markers indicate the amplitudes of the screen surface obtained in the experiment. It can be observed from Figure 10 that the simulated deflection deformation at each moment generally aligns with the experimental results, thereby confirming the accuracy of the numerical simulation.

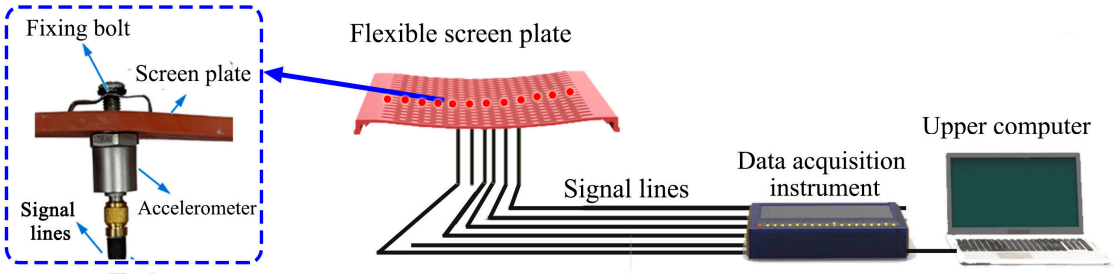


Figure 9. Screen plate amplitude test.

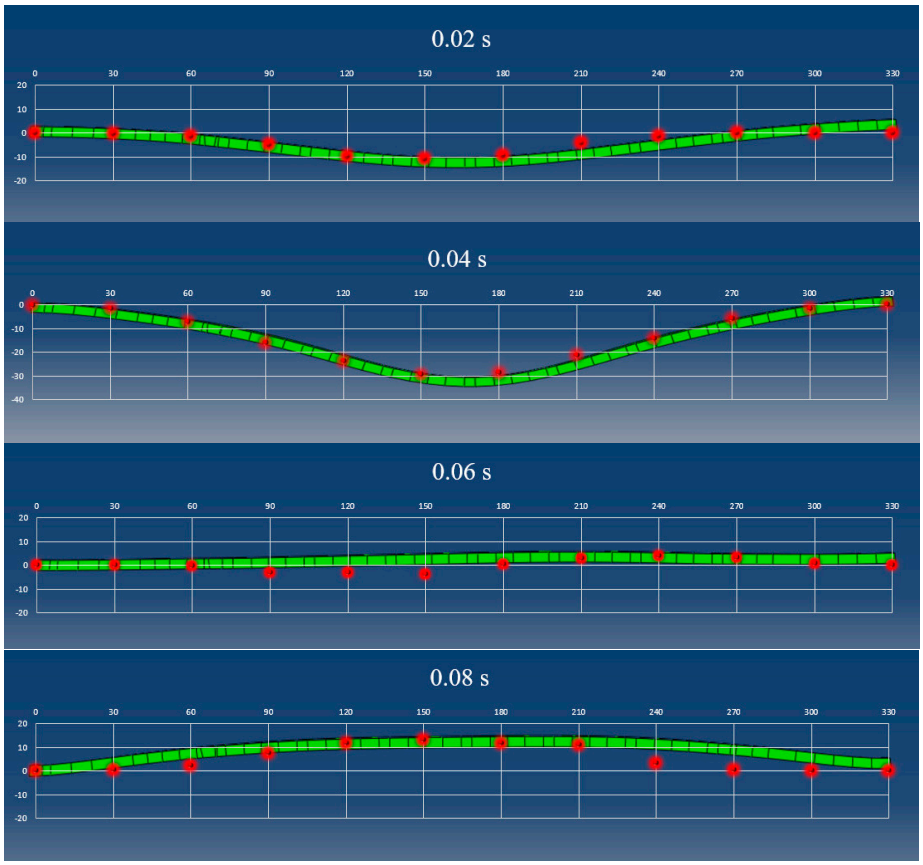


Figure 10. Comparison of deflection between simulation results and experimental results for the screen plate: the red dots represent experimental test results, while the green line represents simulated results.

3.2. Experimental Validation of Screen Frame Dynamics

The vibrating flip-flow screen plate undergoes flexural deformation driven by the driving screen frame and the driven screen frame. Therefore, the accuracy of the simulation of screen frame dynamics cannot be ignored. We compared the motion trajectories at three positions (feed end, center of gravity, and discharge end) of both the driving and driven screen frames between the test results and simulation results. The specific locations of measurement points (1–6) are shown in Figure 11. The tests were conducted using an acceleration acquisition system. The results are presented in Figures 12 and 13. The differences between the test and simulation values at each point are summarized in Table 4, with all errors within a 10% range. The numerical simulation model effectively reproduces the motion trajectories of various points on the flip-flow screen, meeting the requirements for engineering applications.

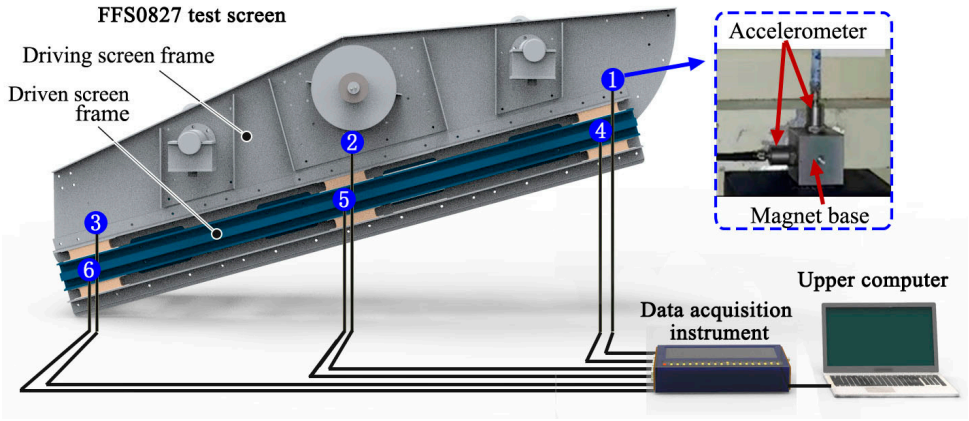


Figure 11. Schematic diagram of experimental measurement points and data acquisition system.

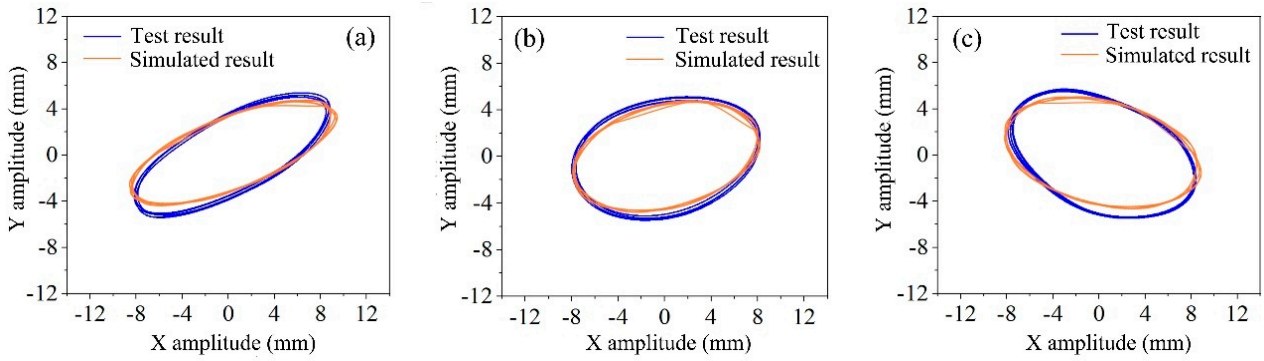


Figure 12. Motion trajectories of various measurement points on the driven screen frame: (**a**) discharge end; (**b**) center of gravity; (**c**) feed end.

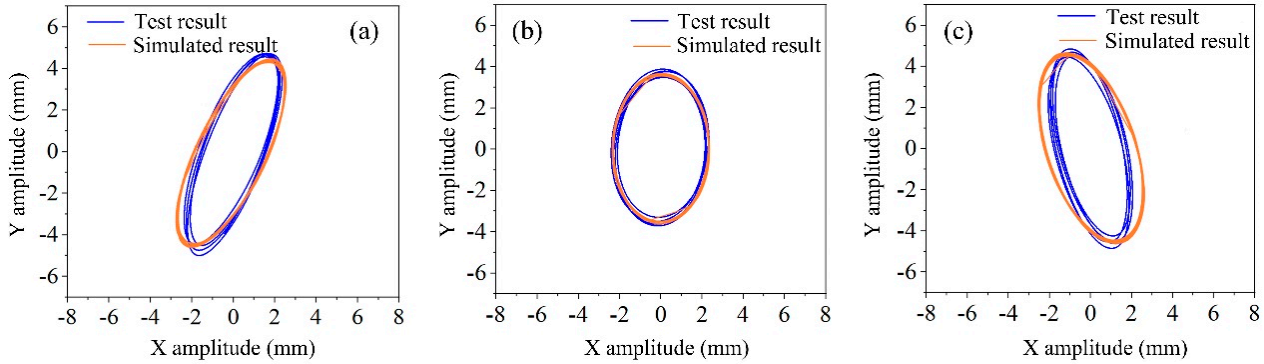


Figure 13. Motion trajectories of various measurement points on the driving screen frame: (**a**) discharge end; (**b**) center of gravity; (**c**) feed end.

Table 4. Comparison of amplitude between virtual prototype and test screen.

Point	Amplitude-x			Amplitude-y		
	Simulation (mm)	Experiment (mm)	Error (%)	Simulation (mm)	Experiment (mm)	Error (%)
1	2.2	2.1	4.7	3.9	4.0	2.5
2	2.0	2.1	4.7	3.4	3.5	2.8
3	2.2	2.0	10	4.5	4.7	4.2
4	8.2	8.0	2.5	5.0	5.3	5.7
5	7.9	8.0	1.3	4.9	5.2	5.7
6	8.8	8.5	3.5	5.2	5.5	5.5

Subsequently, further analysis of the amplitude–frequency characteristics of the experimental screen was conducted, and the experiment measured the amplitude variation within the commonly used working frequency range of 65–100 rad/s. As shown in Figure 14, a comparison of the amplitude–frequency characteristic curves between simulation and experiment indicates a close agreement. The numerical coupling model of the flip-flow screen established in this paper can effectively reflect the amplitude–frequency characteristics of the experimental screen.

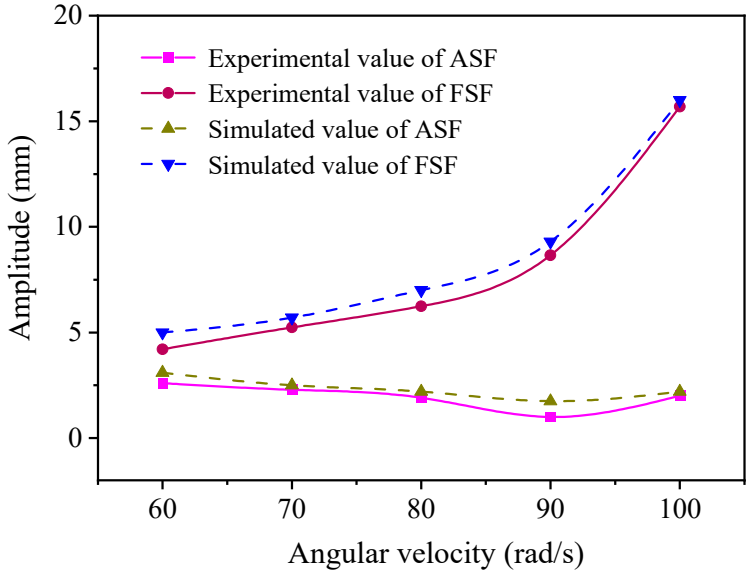


Figure 14. Comparison of amplitude–frequency characteristic curve simulation values and experimental values for the driving screen frame (ASF) and driven screen frame (FSF).

3.3. Experimental Verification of Screening Process

Finally, screening experiments were conducted and compared with simulation results, with the key indicators being screening efficiency and material yield. The experimental screen and its numerical model are depicted in Figure 15. For a more detailed comparison and enhanced reliability of the validation experiments, both the experiment and simulation divided the collection box under the screen into four sections, with each collection of the screened products corresponding to two screen plates. The statistical results of the experimental and numerical calculations are shown in Figure 16. The error between the simulation results of screening efficiency and yield for each section of the screen machine and the experimental results is less than 10%. The screening simulation results of the numerical coupling model essentially meet the requirements for engineering applications.

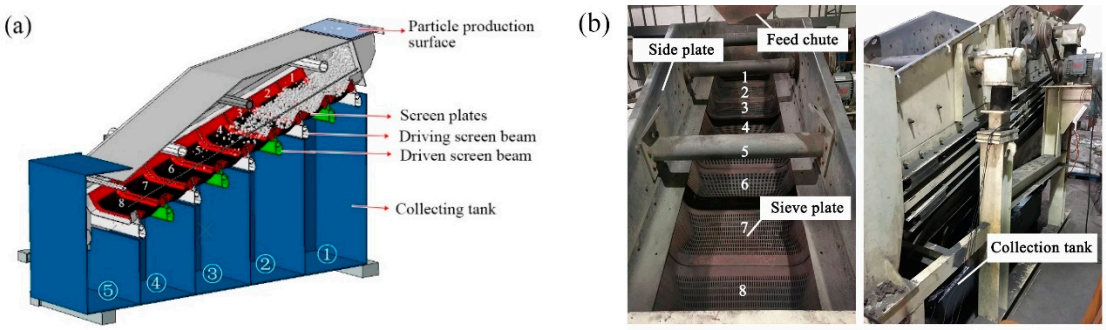


Figure 15. Experimental verification of screening: (**a**) FFS0827 test screen; (**b**) numerical simulation models.

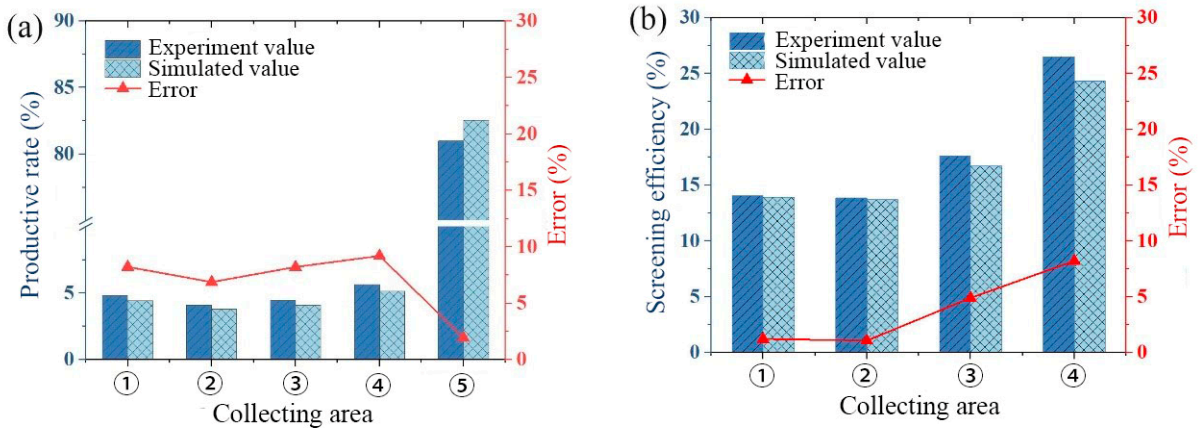


Figure 16. Comparison of results: (**a**) screening yield; (**b**) screening efficiency.

While conducting screening experiments, the relative amplitude of the screen frames was monitored. Figure 17 illustrates the time-domain diagram of the relative displacement of the screen machine in both experimental and simulation scenarios. Both the experiment and simulation involved three processes: (1) the start-up process of the screen machine; (2) the material loading process; and (3) the empty running process. The relative amplitude of the screen machine in both experimental and simulation scenarios is approximately 5.9 mm during empty running and about 5.2 mm under load. The results indicate that the DEM-FEM-MBD coupling model established in this paper can reflect the feedback impact of material load on the dynamics of the screen machine, contributing to the improvement of the accuracy of simulation for heavy-duty screening conditions in vibrating flip-flow screens.

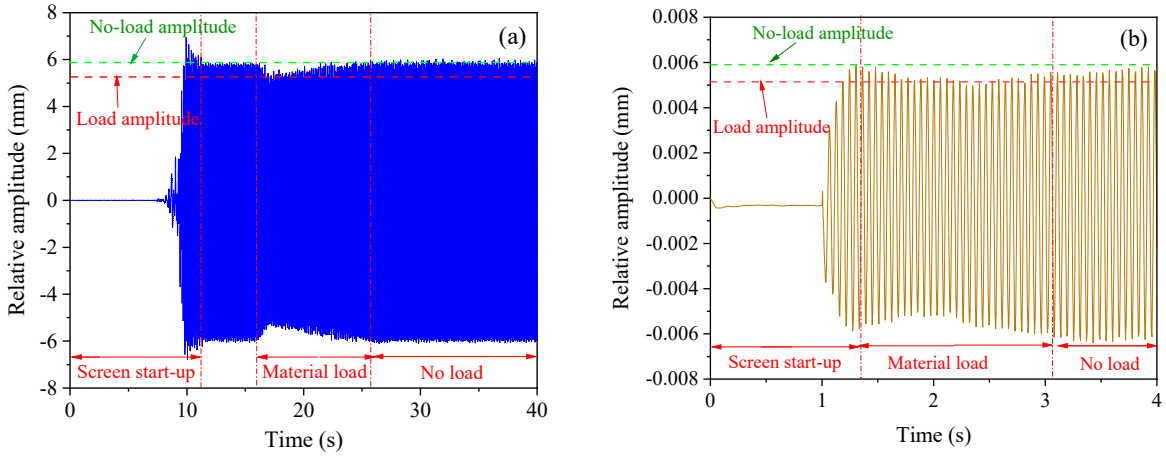


Figure 17. Changes in screen frame amplitude after loading materials: (**a**) experimental results; (**b**) simulation results.

4. Optimization of Flip-Flow Screen Screening

A multi-parameter significance analysis and optimization of the screening process were conducted based on the numerical coupling model DEM-FEM-MBD model for the vibrating flip-flow screen proposed in the previous section.

4.1. Multi-Parameter Significance Analysis of the Flip-Flow Screen

In different processes, the requirements for the performance of the screening machine vary. Some materials with low value or easy screening generally have a larger feed quantity to enhance the processing capacity of the screening machine. On the other hand, for high-value products or processes with higher grading requirements, the focus is more on the screening efficiency of the machine. Therefore, to comprehensively consider the screening

performance of the flip-flow screen, the optimization was conducted with screening efficiency and material velocity as the optimization objectives. The material velocity mentioned here refers to the average velocity of the material on the screen surface throughout the entire process, from feeding to discharging. It can, to some extent, represent the processing capacity of the vibrating screen.

The structure of the flip-flow screen is complex, and there are many adjustable parameters. To improve optimization efficiency, it is crucial to identify the most significant factors influencing the evaluation indicators as optimization targets. In this paper, a mathematical model between influencing factors and evaluation indicators was established based on the response surface method, and the impact of each factor on screening was studied. Five influencing parameters were analyzed, namely, screen surface inclination angle (β), vibration frequency (f), main screen frame amplitude (A_y), main floating screen frame relative amplitude (A_r), and screen surface tensioning amount (δ). The analysis included the screening efficiency (η) and material velocity (v) with various parameters. The experimental plan and results based on the Box–Behnken design [34,35] are shown in Table 5. A total of 43 experiments were conducted, including 5 central replicates for error testing and rationality assessment.

Table 5. Experimental design and results.

No.	A_y (mm)	A_r (mm)	f (rad/s)	β (°)	δ (mm)	v (m/s)	η (%)
1	0	1.5	78.5	20	0	1.10	94
2	4	1.5	78.5	20	0	1.10	94
3	0	5.5	78.5	20	0	1.49	72
4	4	5.5	78.5	20	0	1.51	70
5	2	3.5	58	10	0	0.69	97
6	2	3.5	99	10	0	0.70	99
7	2	3.5	58	30	0	1.98	62
8	2	3.5	99	30	0	2.23	58
9	2	1.5	78.5	20	−4	1.06	95
10	2	5.5	78.5	20	−4	1.40	73
11	2	1.5	78.5	20	4	1.21	91
12	2	5.5	78.5	20	4	1.61	68
13	0	3.5	58	20	0	1.31	84
14	4	3.5	58	20	0	1.30	79
15	0	3.5	99	20	0	1.28	82
16	4	3.5	99	20	0	1.48	75
17	2	3.5	78.5	10	−4	0.67	98
18	2	3.5	78.5	30	−4	2.12	54
19	2	3.5	78.5	10	4	0.71	97
20	2	3.5	78.5	30	4	2.32	51
21	2	1.5	58	20	0	1.10	93
22	2	5.5	58	20	0	1.37	74
23	2	1.5	99	20	0	1.20	92
24	2	5.5	99	20	0	1.51	70
25	0	3.5	78.5	10	0	0.72	96
26	4	3.5	78.5	10	0	0.62	98
27	0	3.5	78.5	30	0	2.01	62
28	4	3.5	78.5	30	0	1.98	57
29	2	3.5	58	20	−4	1.20	85
30	2	3.5	99	20	−4	1.28	83
31	2	3.5	58	20	4	1.40	80
32	2	3.5	99	20	4	1.43	79
33	0	3.5	78.5	20	−4	1.37	76

Table 5. *Cont.*

No.	A_y (mm)	A_r (mm)	f (rad/s)	β (°)	δ (mm)	v (m/s)	η (%)
34	4	3.5	78.5	20	−4	1.41	75
35	0	3.5	78.5	20	4	1.51	74
36	4	3.5	78.5	20	4	1.58	73
37	2	1.5	78.5	10	0	0.58	100
38	2	5.5	78.5	10	0	0.66	93
39	2	1.5	78.5	30	0	1.85	67
40	2	5.5	78.5	30	0	2.22	52
41	2	3.5	78.5	20	0	1.30	84
42	2	3.5	78.5	20	0	1.35	82
43	2	3.5	78.5	20	0	1.32	83

Based on the above results, regression equations were established. Mathematical models such as mean, linear, 2FI, and quadratic were used to fit the experimental data, and the mathematical model between influencing factors and screening efficiency and material velocity were established as shown in Equations (8) and (9):

$$v = 0.43 - 0.12A_y + 0.08A_r - 0.006f + 0.015\beta + 0.02\delta + 0.001A_y f - 0.004A_r\beta - 0.007{A_y}^2 - 0.01{A_r}^2 + 0.004\delta^2 \quad (8)$$

$$\eta = 107.02 + 3.25A_y - 4.04A_r + 0.09f + 0.66\beta - 0.38\delta - 0.09A_y\beta - 0.1A_r\beta - 0.007f\beta - 0.52{A_y}^2 + 0.19{A_r}^2 - 0.04\beta^2 - 0.19\delta^2 \quad (9)$$

Variance analysis of the above models was conducted. The results are shown in Table 6. The p-value reflects the degree of influence of each factor on the evaluation indicators. The smaller the p-value, the more significant the influence of the corresponding parameter on the evaluation indicators. Specifically, $p \leq 0.01$ indicates extremely significant influence; $0.01 < p \leq 0.05$ indicates significant influence; and $p > 0.05$ indicates no significant influence. From Table 6, it can be observed that the p-values for Ay for all evaluation indicators are greater than 0.05, indicating that A_y has no significant impact on all evaluation indicators. In addition, each parameter has a significant impact on the various evaluation indicators. According to the analysis of p-values, the influence of each parameter on material velocity is in the following order: $\beta = A_r > \delta > f > A_y$. The influence of each factor on screening efficiency is in the following order: $\beta > A_r > f > \delta > A_y$. In summary, the most significant factor affecting screening efficiency and material velocity is the screen surface inclination angle.

Table 6. Analysis of experimental variance p-value.

Factor	Material Velocity—p-Value	Screening Efficiency—p-Value
A_y	0.4930	0.1202
A_r	<0.0001	0.0045
δ	0.0016	0.0197
f	0.0034	0.0185
β	<0.0001	<0.0001

4.2. The Five Degrees of Freedom Inclination Model

In Section 4.1, it has been identified that within the given parameter range, the screen surface inclination angle is the most significant factor affecting the screening efficiency and material velocity of the flip-flow screen. Therefore, the next step involves optimizing the inclination angle to achieve higher optimization efficiency. Researchers have previously proposed a banana-shaped flip-flow screen with a curved screen surface, as shown in Figure 18a. This design utilizes a large inclination angle at the feed end to quickly spread the material, allowing for rapid stratification of the material at the feed end. Additionally, it

uses a smaller inclination angle at the discharge end to reduce the material's transfer speed and improve the screening efficiency at the discharge end. However, there has not been further exploration of the variation in the curvature angle for the banana-shaped screen. Current designs typically feature a uniformly changing angle. Yet, the most favorable angle distribution for screening may involve non-uniform changes in the angle.

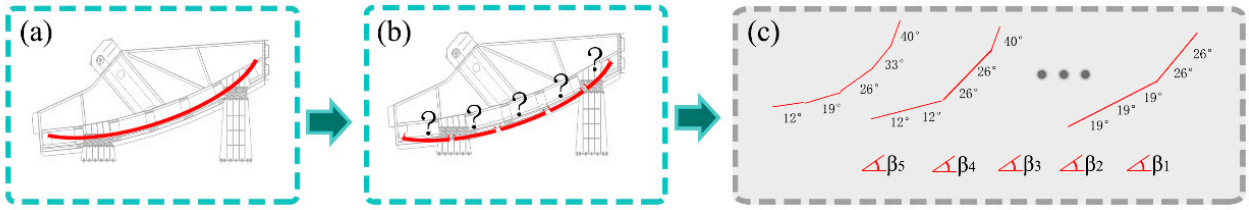


Figure 18. The five-degree-of-freedom inclination (FDFI) model of the flip-flow screen: (**a**) banana-shaped flip-flow screen; (**b**) segmented screen; (**c**) five-degree-of-freedom inclination model.

This study further optimized the inclination shape of the vibrating screen. Regarding the selection of optimization methods, Richter et al. [36] and Roessler et al. [37] provided a comprehensive discussion on parameter calibration and emphasized the advantages of surrogate model-based optimization methods for addressing such problems. Similar considerations apply to this study: (1) DEM-FEM-MBD coupling numerical simulations are computationally expensive, (2) obtaining function gradients related to the problem is challenging, and (3) different operational conditions may require different optimization objectives. Taking into account these factors, this study also chose to utilize surrogate model-based optimization. To be specific, to further investigate which shape (angle distribution) is beneficial for screening, the entire screen surface is divided into five segments, as shown in Figure 18b. Each segment's angle can take any value within the range of 12° to 40°, resulting in a five-degree-of-freedom inclination model (FDFI) of the flip-flow screen, as depicted in Figure 18c. This model allows for any angle distribution on the screen surface. Subsequently, through an optimization process, the inclination angle distribution that corresponds to the optimal screening efficiency and material velocity can be determined.

In the optimization process, a significant number of calculations involving different multi-segment polyline combinations are required based on the numerical coupling model to obtain the optimal combination of inclination angles. However, the coupling process of discrete elements, finite elements, and dynamics imposes high demands on both time and computational power. Additionally, the construction of models for different multi-segment polyline combinations increases the complexity of the problem. Directly using the numerical model for iterative optimization is not practical. Therefore, a surrogate model was established between the FDFI model and screening efficiency as well as material velocity. Subsequently, the surrogate model was iteratively optimized, addressing the computational challenges associated with the extensive calculations.

BP neural networks can learn and represent the nonlinear mapping relationship between inputs and outputs [38]. In this paper, a BP neural network was adopted to establish a FDFI surrogate model based on MATLAB. As shown in Figure 19, the BP neural network is constructed with three layers: the input layer, hidden layer, and output layer. The number of nodes in the input layer is 5, corresponding to the angles β1~β5 from the feed end to the discharge end of the screen. The output layer consists of two nodes, corresponding to the screening efficiency ε and the material velocity v, respectively.

The number of nodes in the hidden layer has a significant impact on the modeling and performance of BP neural networks. An increase in the number of nodes in the hidden layer can enhance the expressive power of the BP neural network, allowing it to better fit the dataset. However, an excessive number of nodes in the hidden layer can reduce

computational efficiency and lead to overfitting issues. The number of neurons in the hidden layer can be determined based on the empirical Formula (10):

$$N = \sqrt{n + m} + a \tag{10}$$

where N is the number of nodes in the hidden layer of the neural network; n represents the number of nodes in the input layer, and m is the number of nodes in the output layer of the neural network. a is an adjustment coefficient between 0 and 10; in this case, the adjustment coefficient was 5. Taking the integer part of the calculation results, the number of nodes in the hidden layer can be chosen as 8. To optimize the neural network structure, a comparison was made of the iterative calculation process with hidden layer counts of 6, 7, 8, 9, and 10, as shown in Figure 20. In this study, the nine nodes mode with minimum mean square error (mse) were chosen.

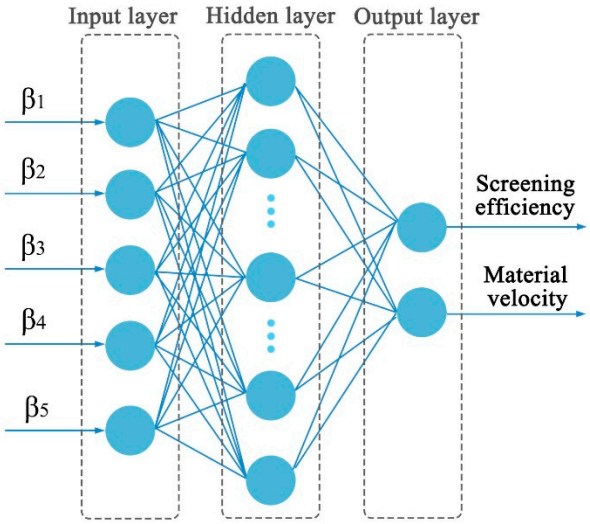


Figure 19. BP neural network structure.

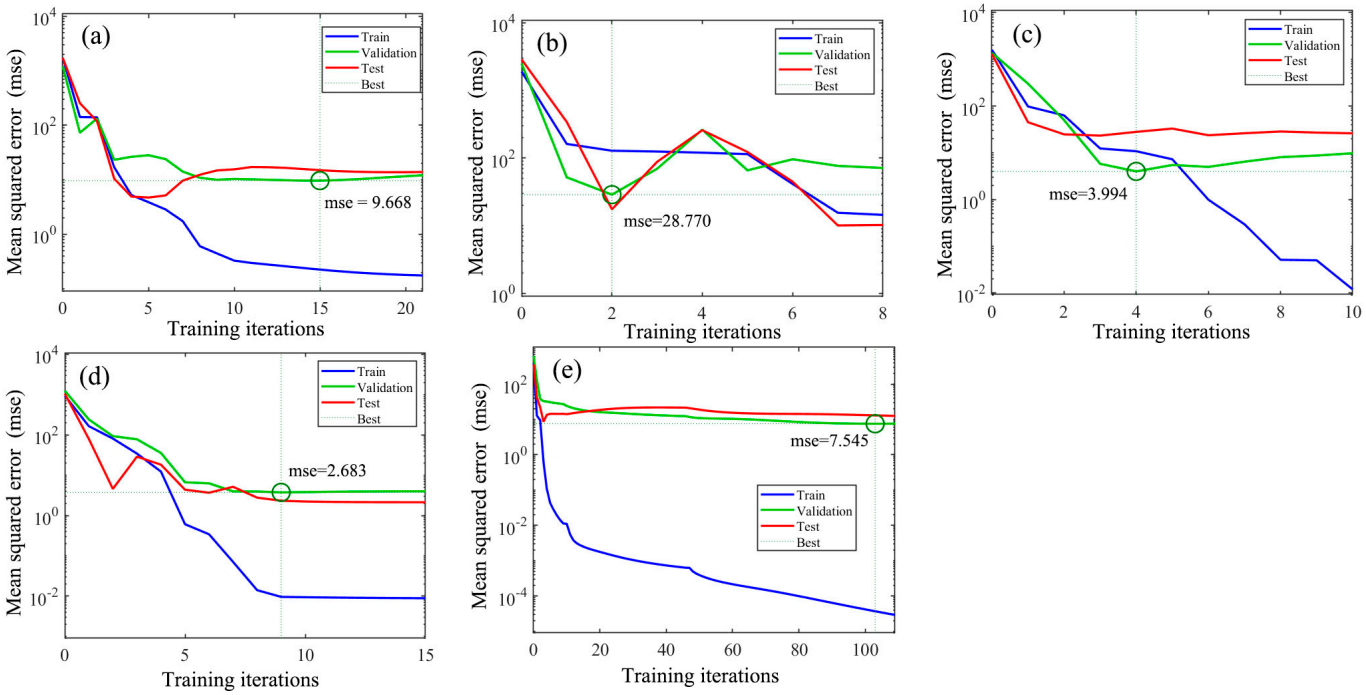


Figure 20. Training process and mean square error (mse) for various numbers of hidden layer nodes: (**a**) 6 nodes; (**b**) 7 nodes; (**c**) 8 nodes; (**d**) 9 nodes; (**e**) 10 nodes.

In total, 80 sets of different FDFI models were selected for simulation experiments, with a feeding speed of 40 kg/s. A total of 80 samples were obtained, and the screening efficiency and material velocity were analyzed as output values corresponding to the samples. These samples were randomly allocated, with 70% used for the training set, 15% for the testing set, and 15% for the validation set during the training process of the BP neural network. The simulated values based on the virtual prototype and the predicted values of the BP neural network for each dataset are shown in Figures 21 and 22. The error between the simulated values based on the virtual prototype and the predicted values of the BP neural network is within 10%, indicating that the trained BP model can effectively describe the relationship between the flip-flow screen's multi-segment incline angle and screening efficiency, as well as material velocity. The BP model can replace numerical models for optimizing the distribution of screen surface angles for flip-flow screens. The established surrogate model for the FDFI flip-flow screen is represented using parallel coordinate axes in Figures 23 and 24.

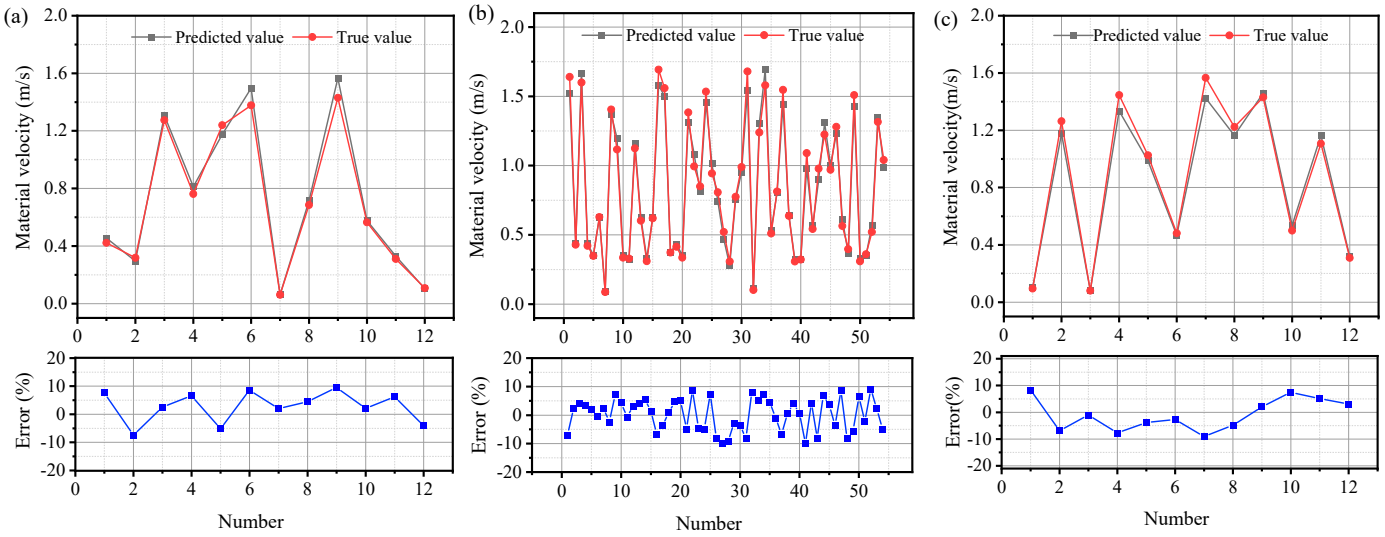


Figure 21. Comparison of the predicted and simulated values of the material velocity: (**a**) testing set; (**b**) training set; (**c**) validation set.

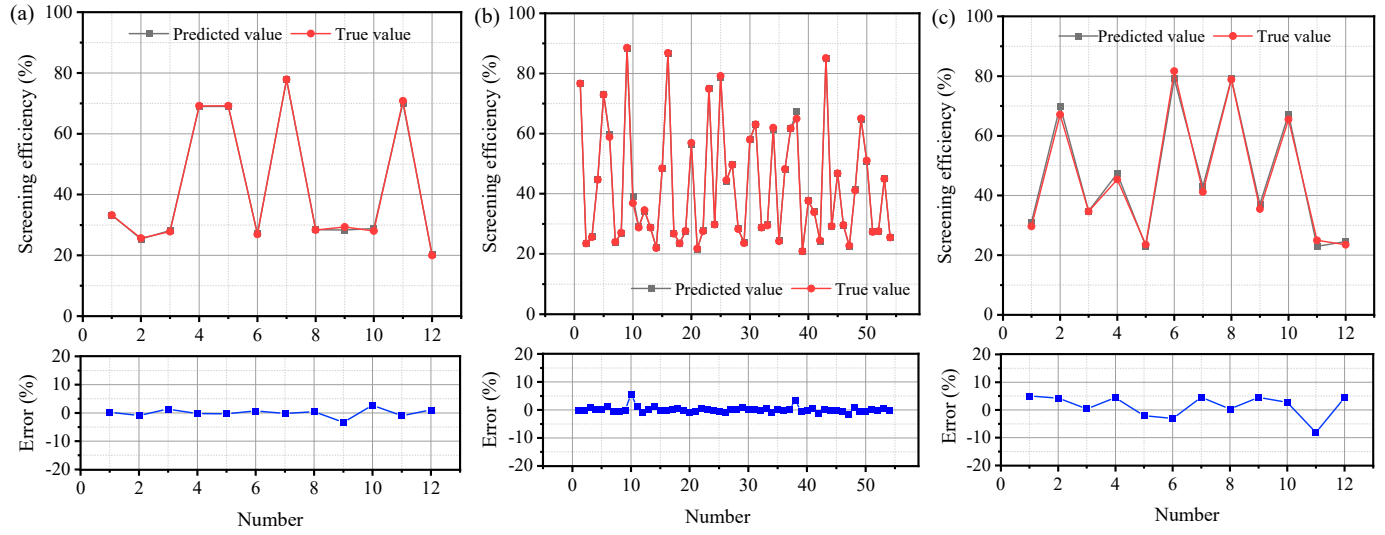


Figure 22. Comparison of the predicted and simulated values of the screening efficiency: (**a**) testing set; (**b**) training set; (**c**) validation set.

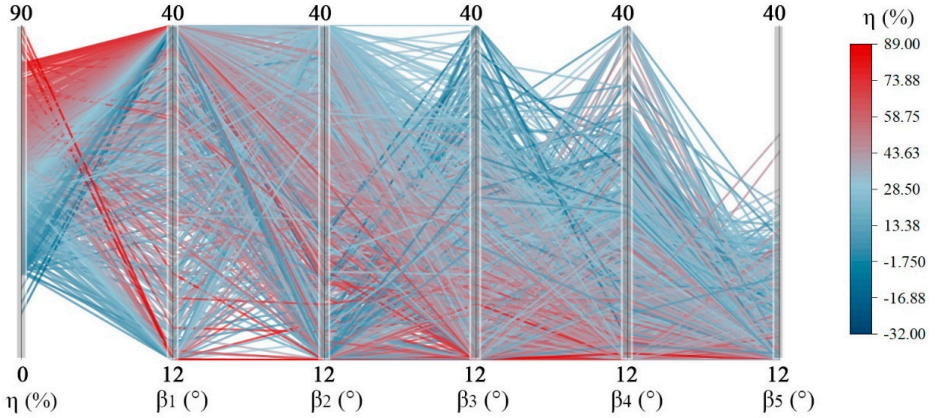


Figure 23. Multistage angle distribution of the screen surface—screening efficiency proxy model.

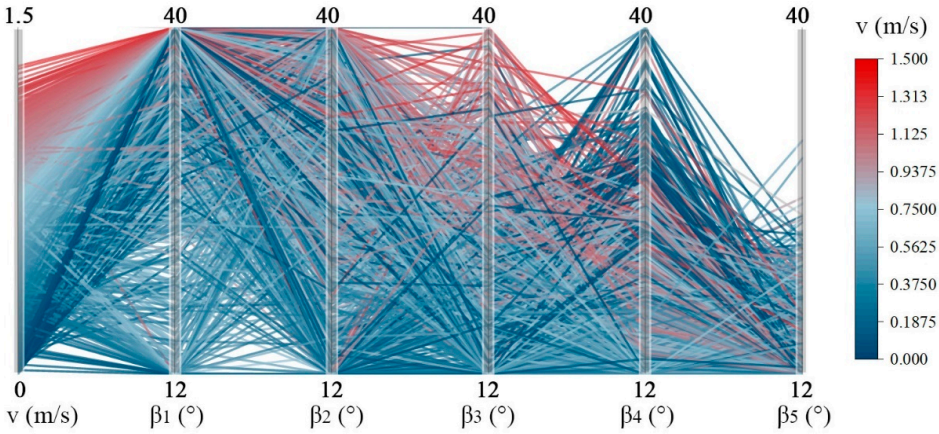


Figure 24. Multistage angle distribution of the screen surface—material velocity proxy model.

4.3. Multi-Operating Condition Optimization of FDFI Model

Optimization was performed based on the surrogate model established in Section 4.2 with the aim of determining the optimal distribution of screen surface incline angles. We constrained screening efficiency as a fixed optimization target then sought the maximum value of material velocity at a certain screening efficiency, thereby transforming the multi-objective optimization problem into a single-objective optimization problem. The optimization process was implemented using the whale optimization algorithm in this study.

The whale optimization algorithm is a heuristic optimization algorithm that simulates the process of whale pods identifying, surrounding, and capturing prey to design the optimization process. The corresponding algorithm includes three strategies as shown in Equations (11) and (12) [39]. The whale optimization algorithm freely adjusts between these three optimization strategies, demonstrating strong global search capabilities.

The adoption of one of the two strategies shown in Equation (11) is determined by a random probability p value ranging from 0 to 1.

$$X(t+1) = \begin{cases} X_{best}(t) - A \cdot D_1 & p < 0.5 \\ D_2 \cdot e^{bl} \cdot \cos(2\pi l) + X_{best}(t) & p \geq 0.5 \end{cases} \quad (11)$$

When $|A| > 1$, the random search strategy as shown in Equation (12) is implemented:

$$X(t+1) = X_{rand}(t) - A \cdot |C \cdot X_{rand}(t) - X(t)| \quad (12)$$

In the equation, D_1 and D_2 are calculated by Equations (13) and (14) respectively, where (t) represents the current iteration number, and X_{best} is the best search position,

$A = (2r - 1) \cdot a$, $C = 2 \cdot r$, and $a = 2 \cdot (1 - t/T)$, where (r) is a random number in the range [0, 1], and T is the maximum number of iterations.

$$D_1 = |C \cdot X_{best}\ (t) - X(t)| \tag{13}$$

$$D_2 = |X_{best}\ (t) - X(t)| \tag{14}$$

Optimization constraints $12^\circ \geq \beta 1 \geq \beta 2 \geq \beta 3 \geq \beta 4 \geq \beta 5 \geq 40^\circ$ were set to ensure that no negative angles are presented and to avoid excessively large or small angle combinations.

In the actual application of flip-flow screens, different production requirements exist based on the screened material. Some processes prioritize screening efficiency, while others aim for higher processing capacity. Therefore, it is necessary to design corresponding parameters for flip-flow screens to achieve the optimal screening effect under different working conditions and process requirements. In this work, optimization was performed for the optimal distribution of screen surface incline angles corresponding to the maximum material velocity at screening efficiencies of 90%, 80%, 70%, and 60%. The optimization results are shown in Table 7.

Table 7. Optimization results.

Screening Efficiencies (%)	β1 (°)	β2 (°)	β3 (°)	β4 (°)	β5 (°)	Material Velocity (m/s)
60	40.0	25.0	15.6	15.6	12.0	0.66
70	38.6	23.7	13.7	13.7	12.0	0.46
80	18.3	13.3	13.3	13.3	13.3	0.28
90	12	12	12	12	12	0.1

In each constraint condition, the surrogate model was randomly solved 1000 times, and the random solution results were compared with the optimization results mentioned above, as shown in Figure 25. The results indicate that the optimization results for each performance requirement are greater than all random results, to some extent demonstrating that each optimization result is close to the global optimum.

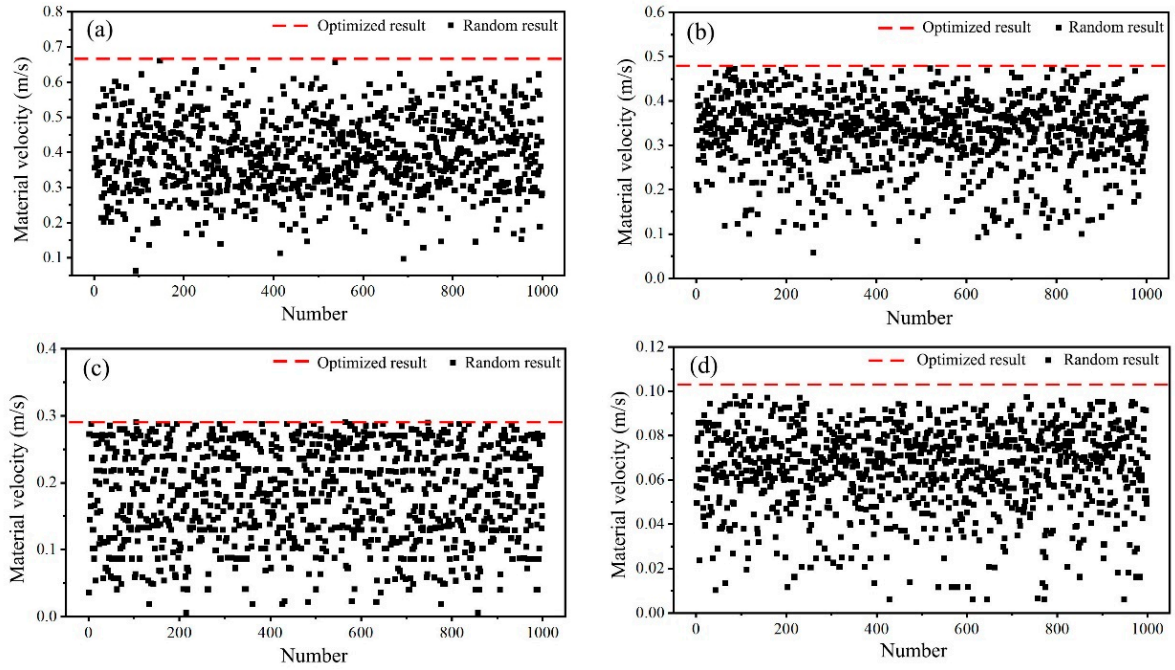


Figure 25. Comparison between optimization results and random results: (**a**) 60%; (**b**) 70%; (**c**) 80%; (**d**) 90%.

Based on the above results, the overall screen surface angle design model for the flip-flow screen was plotted, as shown in Figure 26. It can be observed that for optimization solutions under different operating conditions, the discharge end inclination angles are controlled within a relatively small range. As the processing capacity requirement increases, the gradient of the inclination angle change at the feed end is larger, while the gradient of the angle change at the discharge end is smaller. This is not the uniform gradient of angle change seen in traditional banana flip-flow screens.

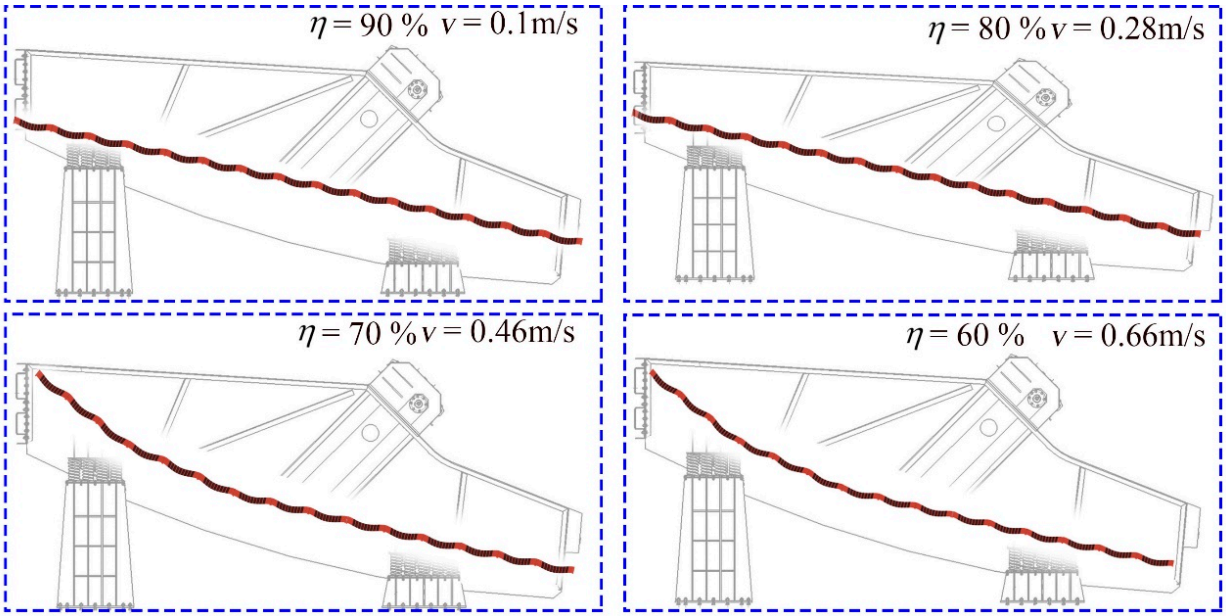


Figure 26. Multi-condition optimization results.

5. Conclusions

Based on DEM-FEM coupling, a dynamic numerical model of the flip-flow screen was established according to the real working conditions of the FFS0827 experimental screen. This implementation realized the DEM-FEM-MBD numerical simulation of the complex system involved in the screening process of the flip-flow screen. To validate the accuracy of the numerical model, tests were performed on the screen frames motion trajectory, amplitude–frequency characteristics analysis, and amplitude testing at various points on the screen plate. The results indicate that the numerical model can reflect dynamic characteristics of the flip-flow screen and flexural deformation process of the screen plate well. Furthermore, a complete screening experiment was conducted on the FFS0827 screening machine. The results demonstrate that the model can accurately reflect the dynamic characteristics of the vibrating flip-flow screen in response to changes in load amplitude. And the simulation error of the screening process is less than 10%, meeting the requirements for engineering applications.

Using the response surface method, the significant impact of each factor of the flip-flow screen on various indicators was clarified. Within the adjustable range of parameters for the existing flip-flow screen, the order of the impact of parameters on material velocity is: $\beta = A_r > \delta > f > A_y$. The order of the impact of factors on screening efficiency is: $\beta > A_r > f > \delta > A_y$. The interaction effects between parameters are relatively small.

A method for the optimization of the screen surface angle distribution has been proposed. First, a five-degree-of-freedom inclination (FDFI) model for the screening surface was established using the discretization approach. Then, A surrogate model of FDFI was established based on a BP neural network, capturing the relationship between FDFI and screening efficiency, as well as material velocity. Finally, the whale optimization algorithm was employed for multi-objective optimization of the surrogate model, yielding

the optimal angle distribution corresponding to the maximum material velocity at different screening efficiencies.

The numerical model of the vibrating flip-flow screen based on DEM-FEM-MBD coupling simulation provides an effective means for improving and developing flip-flow screen equipment. It can also be easily extended to research on various types of vibrating screens and vibratory feeders, as well as other loaded vibrating equipment.

Author Contributions: N.X.: conceptualization, methodology, software, writing—original draft preparation, writing—reviewing and editing; X.W.: supervision; D.L.: investigation, visualization; and data curation; W.Z.: investigation. All authors have read and agreed to the published version of the manuscript.

Funding: This research was funded by the Anhui Province Major Science and Technology Achievements Engineering Research and Development Special Project (No. 202103c08020007) and the Fundamental Research Funds for the Central Universities (No. 2022YJSHH15).

Data Availability Statement: Data are contained within the article.

Acknowledgments: We thank Tiangong Technology Company for providing experimental equipment and venues.

Conflicts of Interest: The authors declare no conflicts of interest.

References

1. Zhou, E.; Yan, G.; Weng, X.; Zhang, Z.; Zhao, P.; Zhang, B. A novel and low cost coal separation process: Combination of deep screening classification and gravity separation. *Powder Technol.* **2020**, *367*, 568–575. [CrossRef]
2. Zhang, B.; Zhu, G.; Lv, B.; Yan, G. A novel and effective method for coal slime reduction of thermal coal processing. *J. Clean. Prod.* **2018**, *198*, 19–23. [CrossRef]
3. Gangfeng, Z.; Jinbo, Z.; Wandong, X.; Shili, L. Banana flip-flow screen benefits coal preparation. *Filtr. Sep.* **2016**, *53*, 38–41. [CrossRef]
4. Dong, F.; Luo, S.; Zhan, C.; Li, T. Discussion on optimization of crushing process in Dongping Hongda Concentrator. *J. Shandong Univ. Technol. (Nat. Sci. Ed.)* **2022**, *36*, 63–66.
5. Zhao, G.; Wang, X.; Lin, D.; Xu, N.; Yu, C.; Geng, R. Study of double-deck vibrating flip-flow screen based on dynamic stiffness characteristics of shear springs. *Minerals* **2021**, *11*, 928. [CrossRef]
6. Lin, D.; Ji, J.; Yu, C.; Wang, X.; Xu, N. A non-linear model of screen panel for dynamics analysis of a flip-flow vibrating screen. *Powder Technol.* **2023**, *418*, 118312. [CrossRef]
7. Akbari, H.; Ackah, L.; Mohanty, M. Performance Optimization of a New Air Table and Flip-flow Screen for Fine Particle Dry Separation. *Int. J. Coal Prep. Util.* **2020**, *40*, 581–603. [CrossRef]
8. Li, H.; Liu, C.; Shen, L.; Zhao, L.; Li, S. Kinematics characteristics of the flip-flow screen with a crankshaft-link structure and screening analysis for moist coal. *Powder Technol.* **2021**, *394*, 326–335. [CrossRef]
9. Geng, R.; Yu, C.; Wang, Y.; Wang, X.; Zhang, X.; Li, R. Effect of External Moisture Content on Screening Performance of Vibrating Flip-Flow Screen and Circular Vibrating Screen. *Minerals* **2023**, *13*, 585. [CrossRef]
10. Wang, W.; Hou, X.; Duan, C.; Mao, P.; Jiang, H.; Qiao, J.; Lu, H. Dynamic model of the flip-flow screen-penetration process and influence mechanism of multiple parameters. *Adv. Powder Technol.* **2022**, *33*, 103814. [CrossRef]
11. Chen, Z.; Wang, G.; Xue, D. An approach to calibration of BPM bonding parameters for iron ore. *Powder Technol.* **2021**, *381*, 245–254. [CrossRef]
12. Fleissner, F.; Gaugele, T.; Eberhard, P. Applications of the discrete element method in mechanical engineering. *Multibody Syst. Dyn.* **2007**, *18*, 81–94. [CrossRef]
13. Chen, W.; Donohue, T.; Katterfeld, A.; Williams, K. Comparative discrete element modelling of a vibratory sieving process with spherical and rounded polyhedron particles. *Granul. Matter* **2017**, *19*, 1–12. [CrossRef]
14. Yu, C.; Geng, R.; Wang, X. A numerical study of separation performance of vibrating flip-flow screens for cohesive particles. *Minerals* **2021**, *11*, 631. [CrossRef]
15. Wu, B.; Zhang, X.; Niu, L.; Xiong, X.; Tang, J. Research on sieving performance of flip-flow screen using two-way particles-screen panels coupling strategy. *IEEE Access* **2019**, *7*, 124461–124473. [CrossRef]
16. Zhang, X.; Wu, B.; Niu, L. Dynamic characteristics of bi-directional coupling between the sag screen surface and the particle population based on DEM. *J. Coal Sci.* **2019**, *44*, 1930–1940.
17. Tang, J.; Niu, L.; Xiong, X.; Jie, S. Viscoelasticity of rubber springs affects vibration characteristics of a flip-flow screen with the high G value. *IEEE Access* **2020**, *8*, 26950–26965. [CrossRef]
18. Chen, B.; Yu, C.; Gong, S.; Wang, X. Dynamic characteristics of LIWELL flip-flow screen panel and particle movement. *Chem. Eng. Sci.* **2021**, *245*, 116853. [CrossRef]

19. Xu, N.; Yu, C.; Gong, S.; Zhao, G.; Lin, D.; Wang, X. Numerical study and multi-objective optimization of flexible screening process of flip-flow screen: A DEM-FEM approach. *Adv. Powder Technol.* **2022**, *33*, 103650. [CrossRef]
20. Dratt, M.; Katterfeld, A. Coupling of fem and dem simulations to consider dynamic deformations under particle load. *Granul. Matter* **2017**, *19*, 49. [CrossRef]
21. Richter, C.; Roessler, T.; Otto, H.; Katterfeld, A. Coupled discrete element and multibody simulation, part I: Implementation, verification and validation. *Powder Technol.* **2021**, *379*, 494–504. [CrossRef]
22. Scheffler, O.C.; Coetzee, C.J. Discrete Element Modelling of a Bulk Cohesive Material Discharging from a Conveyor Belt onto an Impact Plate. *Minerals* **2023**, *13*, 1501. [CrossRef]
23. Bwalya, M.M.; Chimwani, N. Numerical Simulation of a Single and Double-Rotor Impact Crusher Using Discrete Element Method. *Minerals* **2022**, *12*, 143. [CrossRef]
24. Nikishkov, G.P. *Introduction to the Finite Element Method*; University of Aizu: Aizuwakamatsu, Japan, 2004; pp. 1–70.
25. Argyris, J.H.; Balmer, H.; Doltsinis, J.S.; Dunne, P.C.; Haase, M.; Kleiber, M.; Scharpf, D.W. Finite element method—The natural approach. *Comput. Methods Appl. Mech. Eng.* **1979**, *17*, 1–106. [CrossRef]
26. Li, Y.; Castro, A.M.; Sinokrot, T.; Prescott, W.; Carrica, P.M. Coupled multi-body dynamics and CFD for wind turbine simulation including explicit wind turbulence. *Renew. Energy* **2015**, *76*, 338–361. [CrossRef]
27. Lang, H.; Linn, J.; Arnold, M. Multi-body dynamics simulation of geometrically exact Cosserat rods. *Multibody Syst. Dyn.* **2011**, *25*, 285–312. [CrossRef]
28. Yu, C.; Wang, X.; Gong, S.; Pang, K.; Zhao, G.; Zhou, Q.; Xu, N. Stability analysis of the screening process of a vibrating flip-flow screen. *Miner. Eng.* **2021**, *163*, 106794. [CrossRef]
29. Zhou, J.; Zhang, L.; Hu, C.; Li, Z.; Tang, J.; Mao, K.; Wang, X. Calibration of wet sand and gravel particles based on JKR contact model. *Powder Technol.* **2022**, *397*, 117005. [CrossRef]
30. Pan, W.; Hou, X.; Ding, T.; Tang, D. Tangential force model study of lunar dust particles based on Hertz-Mindlin theory and sensor technology. *Sens. Lett.* **2015**, *13*, 176–179. [CrossRef]
31. Santos, C.; Urdaneta, V.; García, X.; Medina, E. Compression and shear-wave velocities in discrete particle simulations of quartz granular packings: Improved Hertz-Mindlin contact model. *Geophysics* **2011**, *76*, E165–E174. [CrossRef]
32. Xu, N.; Tang, S.; Lin, D.; Geng, R.; Wang, X.; Liang, X. Complex granular flows of sticky-wet material on flip-flow screens: Calibration of discrete element simulations. *Particuology* **2024**, *84*, 290–308. [CrossRef]
33. Wu, J.; Liu, C.; Wang, Z. Numerical simulation and parameter optimization of the dynamic characteristics of slack screens. *J. Cent. South Univ. (Sci. Technol.)* **2019**, *50*, 311–320.
34. Wang, L.; Chen, Y.; Jiang, L.; Zhou, H.; Tan, Z.; Du, S. Optimizing Three Kinds of Coagulants Using Plackett-Burman and Response Surface Methodology for Phosphorus Removal from Domestic Sewage. *Pol. J. Environ. Stud.* **2019**, *28*, 877–885. [CrossRef] [PubMed]
35. Ferreira, S.L.C.; Bruns, R.E.; Ferreira, H.S.; Matos, G.D.; David, J.M. Box-behnken design: An alternative for the optimization of analytical methods. *Anal. Chim. Acta* **2007**, *597*, 179–186. [CrossRef] [PubMed]
36. Jin, W.; Li, Z.J.; Wei, L.S.; Zhen, H. The improvements of BP neural network learning algorithm. In Proceedings of the International Conference on Signal Processing, Beijing, China, 21–25 August 2000.
37. Richter, C.; Rößler, T.; Kunze, G.; Katterfeld, A.; Will, F. Development of a standard calibration procedure for the DEM parameters of cohesionless bulk materials—Part II: Efficient optimization-based calibration. *Powder Technol.* **2020**, *360*, 967–976. [CrossRef]
38. Roessler, T.; Richter, C.; Katterfeld, A.; Will, F. Development of a standard calibration procedure for the DEM parameters of cohesionless bulk materials—Part I: Solving the problem of ambiguous parameter combinations. *Powder Technol.* **2019**, *343*, 803–812. [CrossRef]
39. Mirjalili, S.; Lewis, A. The whale optimization algorithm. *Adv. Eng. Softw.* **2016**, *95*, 51–67. [CrossRef]

Disclaimer/Publisher's Note: The statements, opinions and data contained in all publications are solely those of the individual author(s) and contributor(s) and not of MDPI and/or the editor(s). MDPI and/or the editor(s) disclaim responsibility for any injury to people or property resulting from any ideas, methods, instructions or products referred to in the content.